Atomically dispersed magnesium enhancing reactive oxygen species generation over g-C₃N₄ nanosheets for efficient photocatalytic NO removal

Kaining Li [a,b,1], Ningxin Kang [a,1], Xiaofang Li [c], Zhi Wang [a], Ning Wang [d], Yasutaka Kuwahara [b], Kangle Lv [a,*], Hiromi Yamashita [b,*]

[a] *Key Laboratory of Catalysis and Energy Materials Chemistry of Ministry of Education, College of Resources and Environment, South-Central Minzu University, Wuhan 430074, PR China*
[b] *Division of Materials and Manufacturing Science, Graduate School of Engineering, The University of Osaka, 2-1 Yamada-oka, Osaka 565-0871, Japan*
[c] *College of Chemistry and Environmental Engineering, Wuhan Polytechnic University, Wuhan 430023, China*
[d] *College of Environmental Science and Engineering, Beijing University of Technology, Beijing 100124, China*

ARTICLE INFO

ABSTRACT

Photoinduced reactive oxygen species (ROSs)-involving nitrogen oxide (NOx) abatement offers a green way to mitigate environmental air pollution. Developing cost-effective photocatalysts remains challenging yet crucial. Herein, an atomically dispersed Mg-modified g-C₃N₄ nanosheet photocatalyst (xMg-CN) with excellent photoactivity is developed. The 1.0Mg-CN sample delivers a high NO removal rate of 52.3% under visible light irradiation within 30 min, far surpassing the Mg-free analog (CN, 41.2%). Moreover, a suppressed NO_2 byproduct discharge can be achieved. The introduction of Mg single atoms (SAs) alters the charge density distribution on the triazine ring plane of g-C₃N₄, inducing the formation of a built-in electric field, which improves the photoexcited charge carrier separation. Additionally, Mg SAs contribute to the adsorption and activation of O_2 molecules, resulting in enhanced ROSs production, as evidenced by the experiments and theoretical simulations. The findings shed light on the role of SAs in designing highly efficient g-C₃N₄-based photocatalysts for air purification.

1. Introduction

The concentration of atmospheric nitrogen oxides (NOx) continues to rise, as a result of increasing industrial processes and automobile emissions, and is considered to be the main contributor to photochemical smog, ozone depletion, and acid rain [1,2]. Numerous efforts have been devoted to mitigating NOx emissions in recent years [3,4]. However, conventional selective catalytic reduction (SCR) techniques for NOx abatement involve undesired thermal energy consumption, leading to increased greenhouse gas emissions, which is not favorable to environmental sustainability [5,6]. Photocatalytic oxidation NOx removal, driven by inexhaustible solar energy, is regarded to be one of the greenest strategies, especially for the removal of NO at trace level concentration (ppb level) in the air [7,8].

The commercial realization of photo-oxidation for NOx elimination requires the development of photocatalysts with high activity, good stability, and a facile synthetic process. Among the various photocatalysts, metal-free graphitic carbon nitride (g-C₃N₄) is deemed to be an appealing visible light-responsive photocatalyst for this reaction, due to the characteristics of outstanding chemical stability, appropriate band structure, and good biocompatibility [9–13]. Nevertheless, the NO removal photoactivity of pristine g-C₃N₄ is unsatisfactory due to the unsatisfied visible-light utilization capacity, fast recombination of charge carriers, and the resulting inadequate reactive oxygen species (ROSs) production ability. Atomically dispersed metal site modification offers an effective means to enhance the photoactivity of g-C₃N₄ [14–17]. For example, Hu et al. reported Ag single atoms (SAs) anchored on g-C₃N₄ that offered excellent photocatalytic CO_2-to-CO conversion performance, as a result of the boosted transfer of photoinduced electrons because of the Ag SAs introduction [18]. Ou et al. found that single-atom Pt helped suppress the recombination of photo-generated charge carriers of pristine g-C₃N₄, therefore, Pt SAs modified g-C₃N₄ showed excellent photocatalytic H_2 evolution performance and NO photo-oxidation activity [19]. Additionally, Liu and

---

co-workers reported a confined Pd SAs in g-C_3N_4 with carbon vacancies catalyst (Pd-CN-Cv) that exhibited an enhanced NO photo-oxidation performance with a removal rate of 56.3% compared to its counterpart (CN-Cv, 23.5%) under Xe lamp irradiation within 30 min; the results suggested that the single atom modification contributes to the improved light absorption and the prolonged charge carrier lifetime, giving rise to facilitate the formation of $\bullet O_2^-$ and $\bullet OH$, which actively participate in the removal of NO [20]. Considering the scarcity and high cost of noble metals, it is important to develop more cost-effective single-atom-based g-C_3N_4 catalysts.

Magnesium (Mg) is a group II alkaline earth metal element featuring the nondirectionally delocalized 3*s* orbit. In recent years, Mg has been used as the dopant to modify g-C_3N_4 and realize desired results in various catalytic applications, such as electrochemical CO_2 reduction [21], photocatalytic CO_2 conversion [22], and photocatalytic antibiotic degradation [23]. Generally, Mg is present in the form of stable compounds in +2-oxidation state [24]. The Mg^{2+} in the cofactor plays an important role in the photosynthesis system since it has a decent affinity for oxygen-bearing species [25]. The production of ROSs is closely correlated to the adsorption strength of oxygenated intermediates (O*, OOH*); therefore, the introduction of Mg SAs onto g-C_3N_4 is anticipated to facilitate the activation of O_2 molecules and boost the generation of ROSs. However, this aspect has been rarely considered.

In addition, g-C_3N_4 nanosheets show superior photoactivity compared to bulk g-C_3N_4, because the unique 2D structure of g-C_3N_4 allows for the adequate exposure of active sites and a shortened diffusion distance for photo-generated carrier transport from bulk to the surface, along with a prolonged charge-carrier lifetime [26,27]. Herein, an atomically dispersed Mg-modified g-C_3N_4 nanosheet photocatalyst was developed, which functions as an efficient catalyst for photocatalytic NO removal. The impacts of Mg SAs on the g-C_3N_4 photoelectric performance, O_2 adsorption/activation, and ROSs generation were studied experimentally and theoretically. This work might provide fresh insight for designing high-performance single-atom-based g-C_3N_4 materials for sustainable and green air purification.

2. Experimental section

2.1. Materials

Magnesium chloride hexahydrate ($MgCl_2 \bullet 6H_2O$), dicyandiamide (DCDA), and anhydrous ethanol (EtOH) were obtained from Sinopharm Chemical Reagent Co., Ltd. All the chemicals were of analytic grade and used without further purification. Deionized (DI) water was used in all experiments.

2.2. Catalyst preparation

Synthesis of atomically dispersed Mg-modified g-C_3N_4 nanosheets (xMg-CN): xMg-CN samples were prepared via a facile pyrolysis method. Firstly, DCDA (10.0 g) was dissolved in DI water (150 mL). Then, $MgCl_2 \bullet 6H_2O$ was added to the solution, and the mixture was stirred for 30 min. The obtained mixture was transferred into a 200 mL stainless-steel autoclave and held at 160 °C for 12 h. The white powder product was collected by evaporation at 80 °C, followed by calcination for 2 h at 550 °C (heating rate: 10 °C min^{-1}). After being washed with DI water and dried at 60 °C in air, Mg-SAs-modified g-C_3N_4 catalysts were obtained and labeled as xMg-CN, where x represents the added amount (unit: g) of $MgCl_2 \bullet 6H_2O$.

Preparation of control samples (g-C_3N_4 nanosheets and bulk g-C_3N_4): g-C_3N_4 nanosheets (CN) were synthesized using the similar conditions as xMg-CN, but without adding $MgCl_2 \bullet 6H_2O$ (magnesium source). Additionally, bulk g-C_3N_4 (BCN) was prepared by annealing DCDA at 550 °C for 2 h with a heating rate of 10 °C min^{-1}.

2.3. Characterization

XRD patterns of the as-prepared samples were collected on an X-ray diffractometer (D8 ADVANCE Bruker) with a Cu Kα radiation (λ = 0.154 nm). Fourier transform infrared (FTIR) spectra and X-ray photoelectron spectra (XPS) were collected on an infrared spectrometer (NEXUIS-470) and a photoelectron spectrometer (Escalab 250xi, Thermo Scientific), respectively, to study the molecular structure and surface chemical state of the as-prepared catalysts. The sample morphology was observed via a field emission scanning electron microscopy (FESEM, SU8010, Hitachi), and the microstructure and composition of the samples were analyzed on a high angle annular dark-field-scanning transmission electron microscopy (HAADF-STEM, Talos F200S, Thermo Scientific) with an energy-dispersive X-ray spectroscopy (EDS) system. The aberration-corrected HAADF-STEM analysis was performed on a Titan Cubed Themis G2 300 high-resolution transmission electron microscope. Nitrogen adsorption-desorption isotherms were recorded on a nitrogen adsorption apparatus (ASAP-2020, Micromeritics). UV–vis diffused reflectance spectra (DRS) and Photoluminescence (PL) spectra were collected with a UV–vis spectrophotometer (UV2600, Shimadzu) and a fluorescence spectrophotometer (F-4600, Hitachi), respectively. The adsorption of NO onto as-synthesized samples was investigated by means of an *in-situ* DRIFTS apparatus (TENSOR II, Bruker) using the same method as our previous work [28]. Electron spin-resonance (ESR) spectra were collected on an electron paramagnetic resonance (EPR, JES-X320, JEOL) spectrometer. 5,5-dimethyl-1-pyrroline-N-oxide (DMPO) functioned as the trapping agent for $\bullet O_2^-$ and $\bullet OH$, and 2,2,6,6-tetramethylpiperidine (TEMP) was used to trap $^1O_2$. The mass ratio of Mg in the sample was examined by an inductively coupled plasma optical emission spectrometer (ICP-OES, AVIO 200, Perkin Elmer).

2.4. Photoelectrochemical measurement

Transient photocurrent response (TPR) curves, Mott−Schottky plots, and electrochemical impedance spectroscopy (EIS) data were recorded on an electrochemical workstation (CHI760e). Catalyst-coated ITO electrode, Pt wire, and calomel electrode were employed as the working, counter, and reference electrodes, respectively. An LED lamp (420 nm) was used as the light source for collecting the transient photocurrent response data.

2.5. Photocatalytic NO removal performance evaluation

The NO photo-oxidation ability test was conducted via a continuous flow testing system with a reactor (volume: 4.5 L), using an LED lamp as the light source (λ > 420 nm). Specifically, 200 mg of photocatalyst was added to 30 mL of DI water, followed by ultrasonication treatment for 30 min. Then, the suspension was spread onto a glass dish (diameter: 12 cm) and dried in an oven (60 °C). The resulting catalyst film was subsequently put into a rectangular reactor prior to the photocatalytic reaction. Before turning on the lamp, NO gas and air were mixed in a gas bottle and pumped into the reactor. After reaching gas adsorption-desorption equilibrium (the NO concentration was maintained at ca. 550 ppb), the LED lamp was switched on to trigger the photocatalytic reaction. An online chemiluminescence NOx analyzer (Thermo Scientific, 42i-TL) was used to monitor the dynamic concentration variation of NO and NO_2—. The NO purification ratio (η) was determined using the equation: η (%) = (1 − C/C_0) × 100%, with C and C_0 representing the NO concentration in the outlet and import, respectively. The NO_2 conversion rate was determined using the formula $[NO_2]_{yield}$ (%) = $[NO_2]_{yield}/(C_0 − C)$.
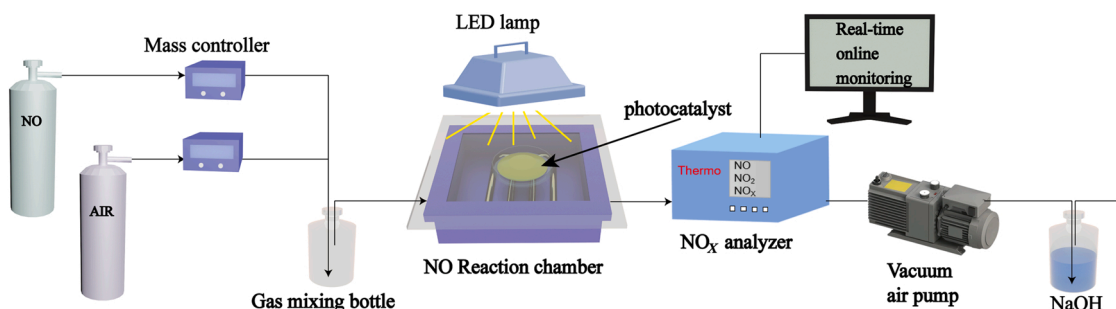
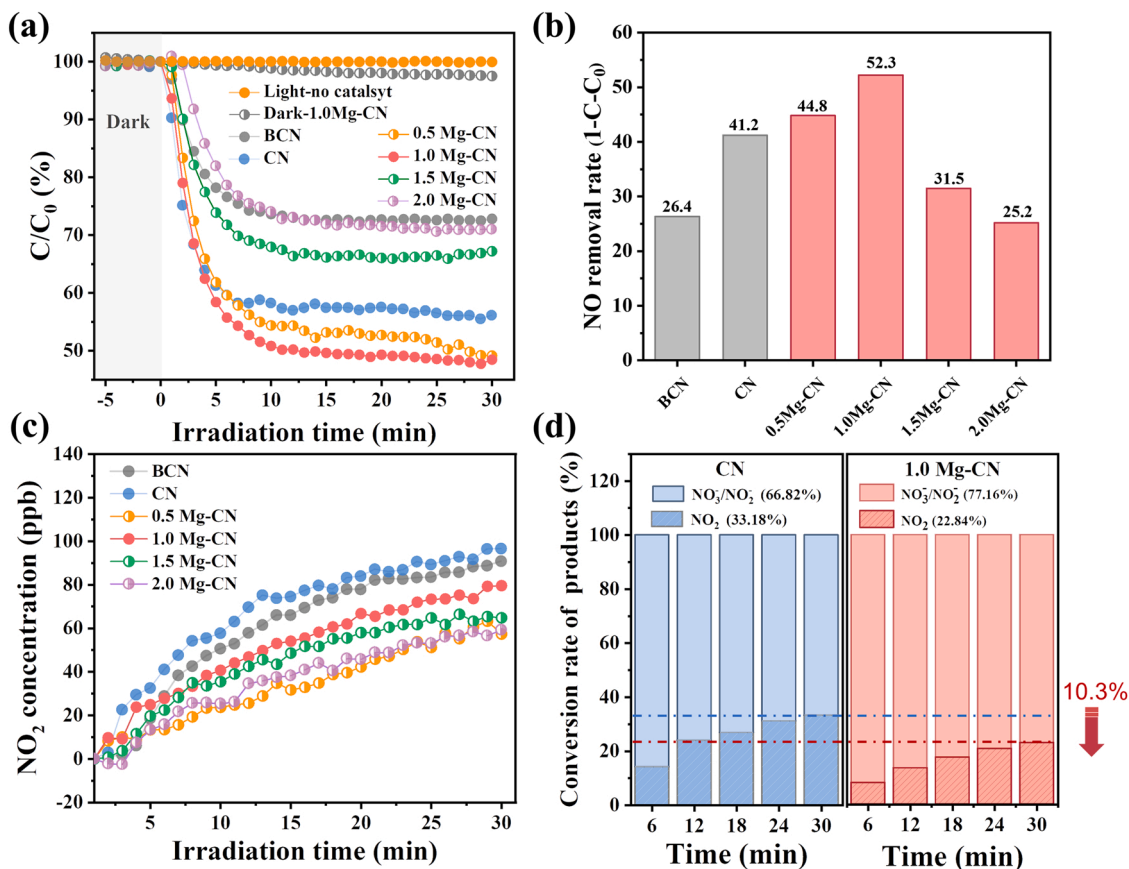**Scheme 1.** Schematic illustration of the photocatalytic NO oxidation test setup.

Fig. 1. (a) NO photo-oxidation removal curves of BCN, CN, and xMg-CN, (b) the corresponding NO removal rate, and (c) NO$_2$ evolution curves of the as-synthesized catalysts. (d) Relative intensity of product conversion in photocatalytic NO removal reaction within 30 min for CN and 1.0Mg-CN.

3. Results and discussion

3.1. Photocatalytic NO oxidation performance evaluation

The visible-light-driven photocatalytic NO removal test of as-synthesized samples was performed using a continuous flow reaction system, as illustrated in Scheme 1. After NO adsorption-desorption reached equilibrium in dark conditions, the lamp was switched on to start the photocatalytic reaction. With the extension of irradiation time, the NO removal plots for all the samples exhibited a decreasing trend at first and then became steady (Fig. 1a). The corresponding NO photocatalytic removal rates were illustrated in Fig. 1b. BCN showed poor photoactivity with a NO removal rate of 26.4% conceivably due to the small BET surface area of only 13.0 m^2 g^{-1} (Table S1) and the resulting limitation of surface accessibility. A moderate NO photo-purification rate was seen for pristine CN catalyst, which is associated with the

easy recombination of electron-hole pairs. Notably, 0.5Mg-CN and 1.0Mg-CN samples exhibited a higher NO removal rate in comparison to the Mg-free analog, CN, which resulted from optimized structural and electronic features, as will be discussed later. Especially, 1.0Mg-CN showed the highest performance improvement, with the NO removal rate reaching 52.3%, much higher than that of CN (41.2%). However, the excessive addition of Mg was detrimental to photoreactivity due to the severe structure destruction of in-plane tris-triazine moieties of g-C$_3$N$_4$ during the hydrolysis or thermal polymerization, which explains the reason that the photoactivity of 1.5Mg-CN and 2.0Mg-CN is lower than that of 1.0Mg-CN [13]. To verify the occurrence of photocatalytic reactions, control experiments were conducted. As shown in Fig. 1a, there was no significant change for the NO concentration in the absence of catalyst under irradiation (Light-no catalyst curve) or in the presence of 1.0Mg-CN catalyst but in the dark (Dark-1.0Mg-CN curve). These results suggested that both catalyst and irradiation are necessary
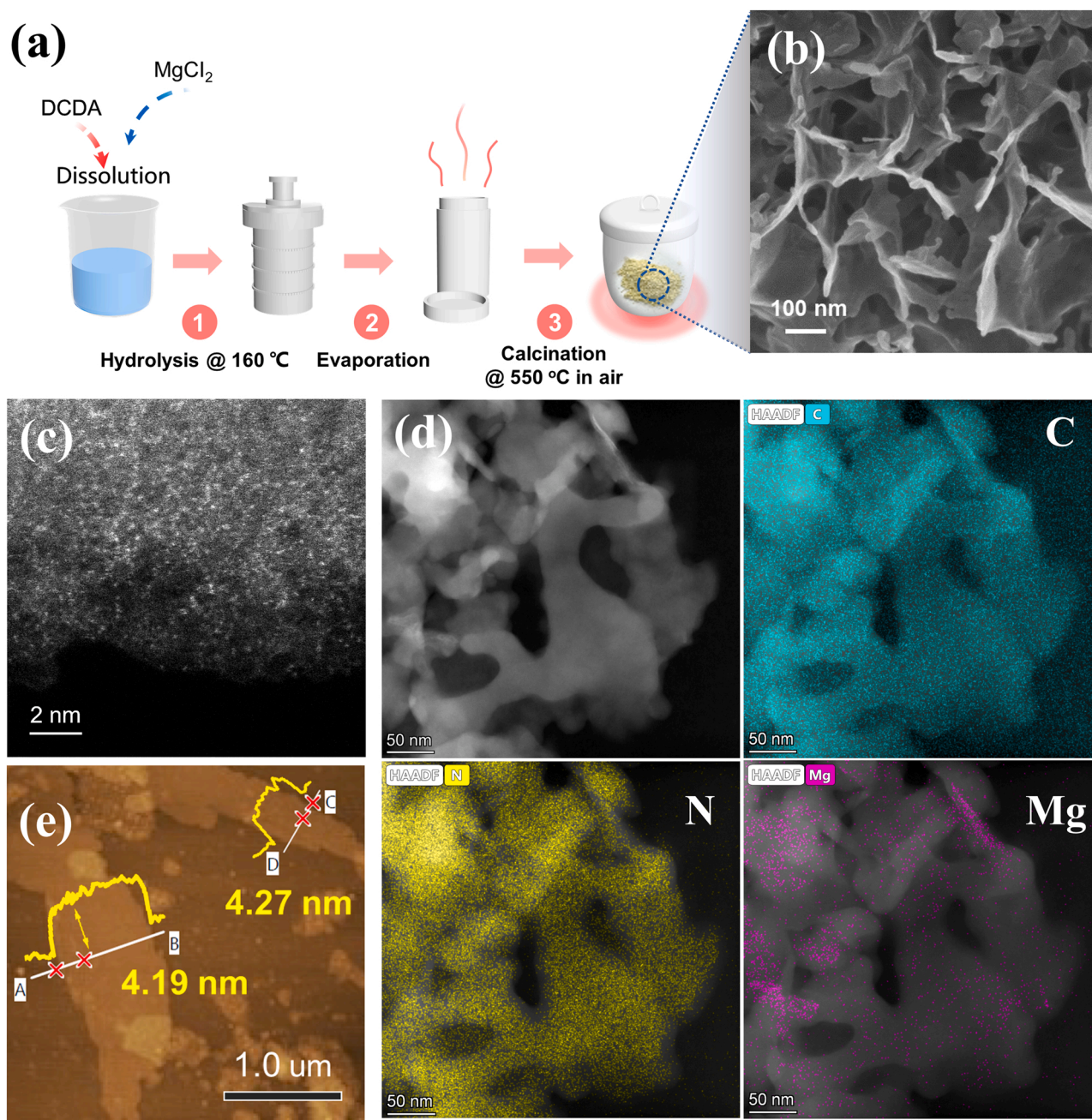
Fig. 2. (a) Schematic illustration of the preparation process for 1.0Mg-CN, (b) SEM image, (c) AC HAADF-STEM image, (d) HAADF-STEM image and the corresponding EDS mapping images of C, N, and Mg elements, and (e) AFM image for 1.0Mg-CN catalyst.

conditions for initiating photocatalytic NO oxidation. Table S2 presents a summary of the photocatalytic NO removal performances of the catalyst in this work and representative catalysts in the literatures. The result indicates that 1.0Mg-CN in this work shows a competitive NO photo-oxidation activity. Apart from the removal rate of NO, the production of by-product NO_2 is also an important evaluation factor for NO photo-oxidation removal performance, as NO_2 is more toxic than NO. The NO_2 generation of all Mg-modified samples was lower than that of CN (Fig. 1c), and the NO-to-NO_2 conversion rate over 1.0Mg-CN sample has been suppressed by 10.3% (Fig. 1d), indicating the positive effect of Mg species on NO_2 emission inhibition.

In addition, the durability of the best-performing sample (1.0Mg-CN) was examined. As seen in Fig. S1a, after repetitive tests for 5 runs, the decrease of NO removal rate was less than 6.6%, suggesting the relatively high stability of the catalyst. N_2 physisorption measurement revealed that the original type-IV adsorption-desorption isotherm of 1.0Mg-CN sample remained unchanged after 5 cycling experiments (Fig. S1b), demonstrating the pore structure type could be well maintained. Whereas, the BET surface area of the used sample showed a decrease compared to the fresh sample (Table S1), probably due to the congestion of the by-product and pore block, as a result, a slight deactivation of the catalyst was caused. Furthermore, XRD and FTIR analyses indicated that chemical structures and components of the catalyst could be retained upon the reusability test (Figs. S1c and S1d), reaffirming the potential for further practical application.

3.2. Physicochemical properties of as-prepared samples

The synthesis procedure of 1.0Mg-CN is depicted in Fig. 2a (see experimental section for details). The morphology of 1.0Mg-CN was
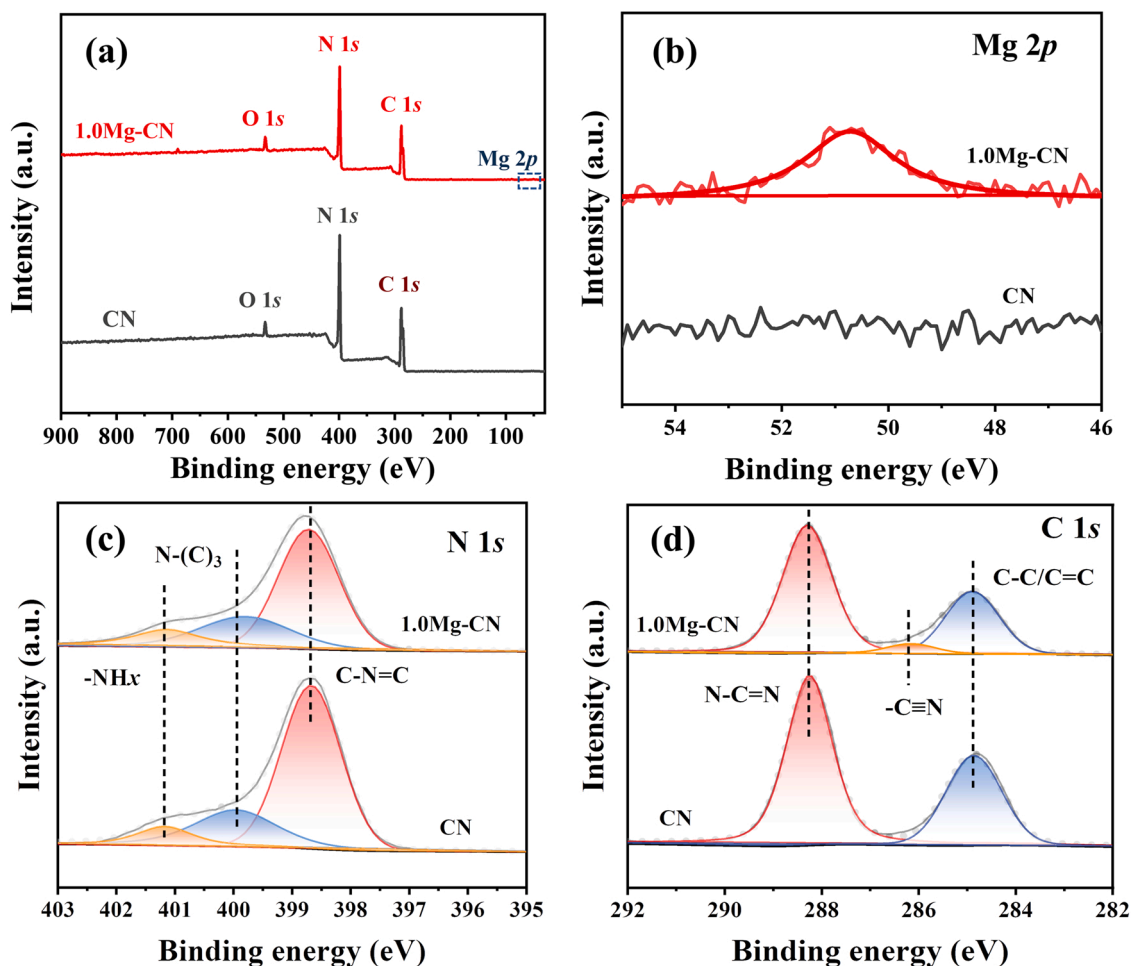
Fig. 3. (a) XPS survey of CN and 1.0Mg-CN, and (b) corresponding partial enlarged XPS spectrum of Mg 2p in (a). XPS spectra of (c) N 1s and (d) C 1s for CN and 1.0Mg-CN.

examined by scanning electron microscopy (SEM), aberration-corrected high-angle annular dark-field scanning transmission electron microscopy (AC HAADF-STEM), and atomic force microscopy (AFM) observations. 1.0Mg-CN exhibited a porous and sheet-like structure (Fig. 2b). Atomic dispersion of Mg was clearly observed and confirmed by AC HAADF-STEM measurement (Fig. 2c), which showed numerous isolated bright spots corresponding to single Mg atoms. As indicated by STEM and the corresponding EDS mapping images (Fig. 2d), no metal nanoparticles were found, and Mg atoms were well distributed on the nanosheet region that contains carbon and nitrogen atoms, verifying the successful introduction of Mg SAs onto g-C_3N_4 frameworks. The thickness of lamellar 1.0Mg-CN was measured to be ca. 4 nm (Fig. 2e), which corresponded to 10 molecular layers of g-C_3N_4 [29]. Similarly, the Mg-free sample, CN, showed thin and twisted flakes (Fig. S2).

The crystal and molecular structures of as-prepared samples were identified via XRD and FTIR spectroscopy. As depicted in Fig. S3a, all the samples showed two characteristic peaks at 12.9° and 27.7°, which are attributable to the in-plane structural repeating units of tri-s-triazine ((100) crystal plane) and interlayer stacking of C-N heterocycles ((002) crystal plane), respectively. No obvious peaks assignable to magnesium compounds (e.g., Mg_3N_2 and MgO) were observed, indicating the good dispersion of Mg atoms. It is noted that the intensity of (100) and (002) peaks of xMg-CN samples steadily decreased with the increased Mg precursor addition amount, due to the destruction of the in-plane aromatic structure. In FTIR spectra (Fig. S3b), xMg-CN showed similar absorption peak patterns as CN and BCN, suggesting the basic skeleton of carbon nitride can be moderately maintained even after Mg

SAs introduction. Meanwhile, a faint peak located at 2170 cm^{-1} attributed to the asymmetric stretching vibration of the cyano group (–C≡N) was seen for xMg-CN, which originated from the opening of the triazine rings, as a result of the interaction of $MgCl_2$•$6H_2O$ and DCDA during the thermal polymerization process [13]. Additionally, N_2 adsorption-desorption measurement was conducted to determine the specific surface area (S_{BET}) and pore characteristics of BCN, CN, and 1.0Mg-CN catalysts. As shown in Fig. S4a, typical type-IV N_2 sorption isotherms with H3-type hysteresis loops were seen for these samples, suggesting the presence of mesopores, which is well matched with the pore size distribution results (Fig. S4b). Benefiting from the unique nanosheet structure, CN and 1.0Mg-CN displayed increased S_{BET} values (Table S1), as compared to BCN. However, because of the partial Mg intercalation, the S_{BET} and pore volume of 1.0Mg-CN were slightly smaller than those of CN; this result is similar to the case of Ca-insertion into CN as reported in previous literature [30].

XPS spectra were further used to acquire the structural information of the samples. XPS survey spectra of CN and 1.0Mg-CN showed the existence of O, C, and N elements (Fig. 3a), while 1.0Mg-CN exhibited a characteristic peak identified at 50.7 eV in the high-resolution Mg 2p XPS spectra, which indicates that Mg is successfully introduced into g-C_3N_4 (Fig. 3b) [31,32]. The content of Mg was quantified to be 0.052 wt % by ICP-OES. The peaks of N 1s located at 398.7, 400.0, and 401.2 eV refer to C–N=C, N–(C)$_3$, and –NH$_x$ groups (Fig. 3c), respectively [33, 34]. In contrast to CN, a new peak at 286.2 eV was observed in C 1s spectra for 1.0Mg-CN (Fig. 3d) [13,35], which is associated with the formation of –C≡N, and the result is well matched with FTIR data.
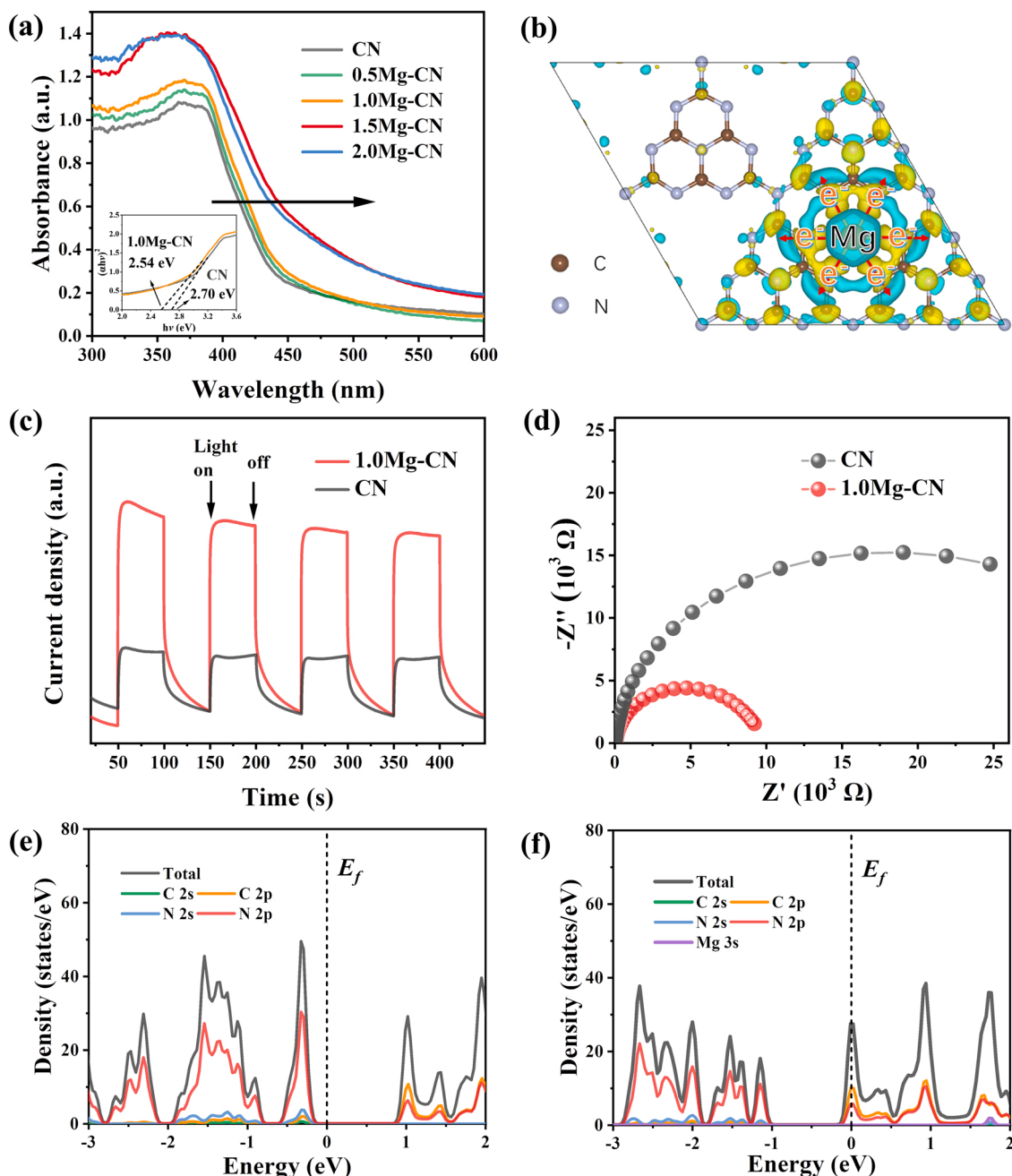
Fig. 4. (a) UV–vis DRS spectra of the as-synthesized samples. The inset shows Tauc plots of CN and 1.0Mg-CN. (b) Charge density difference of Mg SAs-modified g-C_3N_4 (001) with an isosurface of $1.8*10^{-3}$ e/Å^3. (The yellow and cyan regions represent the charge accumulation and depletion, respectively.) (c) Transient photocurrent curves, (d) EIS Nyquist plots of CN and 1.0Mg-CN. Density of states (DOS) of CN (e) and Mg-CN (f).

Specifically, under high-temperature treatment, the introduction of MgCl₂•6H₂O leads to the fracture of C–N≡C, leading to the formation of –C≡N. Such structural changes in g-C_3N_4 frame have also been observed in the ionothermal synthesis process with the assistance of other chlorides (NaCl or CaCl₂) [13,34].

3.3. Photoelectrochemical properties analysis

UV–vis DRS was used to evaluate the optical absorption capacity of the photocatalysts. Obviously, in the presence of Mg, the absorption edge of CN showed a redshift (i.e., 1.0Mg-CN sample) (Fig. 4a), indicating the promoted visible-light harvesting ability of *x*Mg-CN catalysts. Additionally, the corresponding Tauc plot (inset of Fig. 4a) revealed the band gap value decreased from 2.70 eV (CN) to 2.54 eV (1.0Mg-CN).

The reduced band gap of CN after introducing Mg SAs is also confirmed by calculated band gap data (Fig. S5). The difference in calculated band gap value and experimental value is caused by the limitation of DFT calculations. Fig. S6 showed the Mott-Schottky plots of 1.0Mg-CN and CN samples; the positive Mott-Schottky slope suggested that they have n-type semiconductor characteristics [36,37]. Therefore, the observed flat-band potential was approximately equivalent to the conduction band edge (E_{CB}) potentials. The E_{CB} of 1.0Mg-CN was estimated to be −1.23 V vs. Ag/AgCl (pH = 6.7), namely, −0.64 V vs. RHE, according to the converted equation ($E_{Ag/AgCl} = E_{RHE} - 0.059$ pH − 0.197) [38]. Similarly, the E_{CB} of CN was determined to be −0.56 V. Combining the obtained values of bandgap and E_{CB}, the energy band positions of 1.0Mg-CN and CN were confirmed, as illustrated in Fig. S7 [39]. Apparently, in comparison with CN, 1.0Mg-CN exhibited a narrower
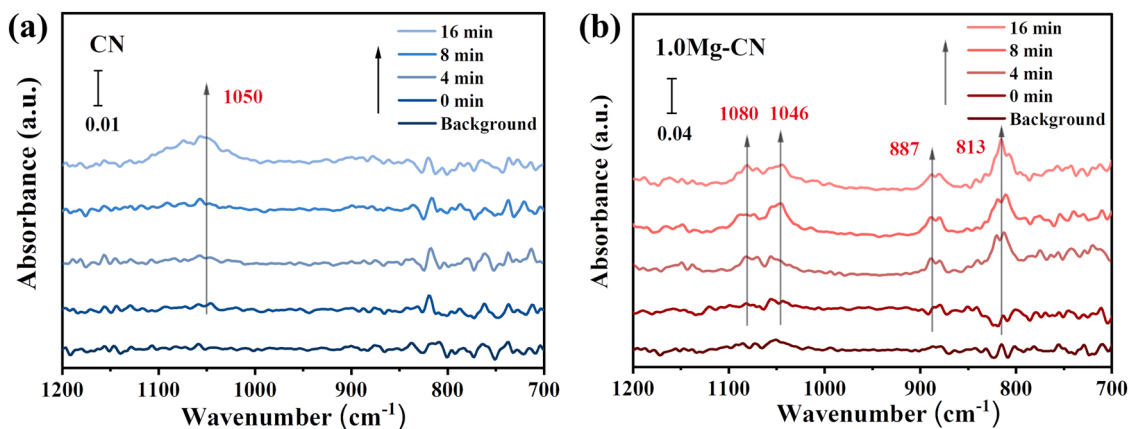
Fig. 5. *In-situ* DRIFTS spectra for NO adsorption for (a) CN and (b)1.0Mg-CN.

band gap and a more negative conduction band potential, implying the extended light-responsive range and the enhanced driving force for oxygen activation to produce $\bullet O_2^-$.

To provide information on the changes in the electronic structure of g-C_3N_4 caused by Mg addition, charge difference distribution analysis was conducted, and the results were shown in Fig. 4b. The introduction of Mg promoted the charge delocalization degree, forming some specific electron-rich regions located at the adjacent N atoms. As a result, in the triazine ring plane of g-C_3N_4 with Mg introduction, a locally built-in electric field was formed due to the presence of the potential difference. The built-in electric field would facilitate the spatial charge separation, which is rather desired to achieve intensive electron exchange between the reactant molecule (NO and O_2) and the catalyst during the photocatalytic processes [29,30].

Furthermore, to understand the positive effects of the built-in electric field induced by Mg single atom on the charge dynamic behavior of g-C_3N_4, steady-state photoluminescence (PL), and transient photocurrent response (TPR) measurements were performed. CN as a prototype material was used to compare with 1.0Mg-CN. As shown in PL results (Fig. S8), the emission intensity observed from 1.0Mg-CN was much lower than CN, implying the low radiative recombination rate of photogenerated carriers. This result was also evidenced by the TPR curves (Fig. 4c); the photocurrent intensity of 1.0Mg-CN was around 3 times higher than the value of CN. The increased photocurrent intensity indicates that there are more photo-excited carriers available for the photocatalytic reaction in 1.0Mg-CN as compared to that of CN [40]. Moreover, 1.0Mg-CN exhibited a much smaller arc radius of the EIS Nyquist plot compared to CN (Fig. 4d), indicative of the apparent reduction of the electron-transfer resistance, which originates from the modulation of Mg atom introduction for improving the conductivity of g-C_3N_4. Such a result was supported by the density of states (DOS) data for CN and 1.0Mg-CN. As depicted in Fig. 4e and 4f, in contrast to CN, the overlap of partial DOS with Fermi level can be observed over 1.0Mg-CN, reflecting its strengthened conductivity [41].

3.4. Photocatalytic NO removal mechanism

For further elucidation about the interaction between reactant NO and the catalysts, DRIFTS was employed to examine the adsorption behavior of NO onto the catalysts, which is the incipient stage before the photoinduced charge-involved reaction. The time-dependent *in-situ* DRIFTS result (Fig. 5a) of NO adsorption over CN showed one absorption peak centering at 1050 cm^{-1} that is identified as bidentate nitrates [29]. By contrast, additional bands associated with nitrates (1080 and 813 cm^{-1}), and chelated nitrites (887 cm^{-1}) were seen over 1.0Mg-CN sample (Fig. 5b) [8,42,43]. Obviously, in comparison to the Mg-free sample (CN), 1.0Mg-CN showed more intense and varied DRIFTS peaks, implying a strong interaction occurs between NO molecule and 1.0Mg-CN.

Generally, photogenerated reactive oxygen species that originate from oxygen activation reactions are regarded as the important species contributing to pollutant degradation [44–46]. The content of generated ROSs has a substantial effect on the removal efficiency and conversion pathway of the pollutants [47]. Herein, theoretical simulation analysis was conducted to illustrate the O_2 adsorption and activation behaviors on the models of CN and Mg-CN. As shown in Fig. 6a and 6b, it can be clearly seen that Mg-CN shows a much larger adsorption energy (E_{ads} = –3.57 eV) toward the O_2 molecule when compared to the value of the Mg-free sample (CN, E_{ads} = –1.67 eV) (see Table S3 for details). One of the reasons that contributes to the dramatic increase of E_{ads} is the change of O_2 adsorption behavior from weak physisorption (CN) to robust chemisorption (Mg-CN), as a result of Mg introduction. It is worth noting that the length of O=O bond in O_2 that is absorbed on Mg-CN becomes 1.390 Å, which is longer than those of CN (1.239 Å) and free O_2 (1.235 Å); this result confirms the benefits of Mg introduction on promoting the O_2 activation.

Differential charge density allows us to further understand the reason for the elevated O_2 adsorption and activation at the electronic level (Fig. 7). The electron cloud in yellow and cyan represents the
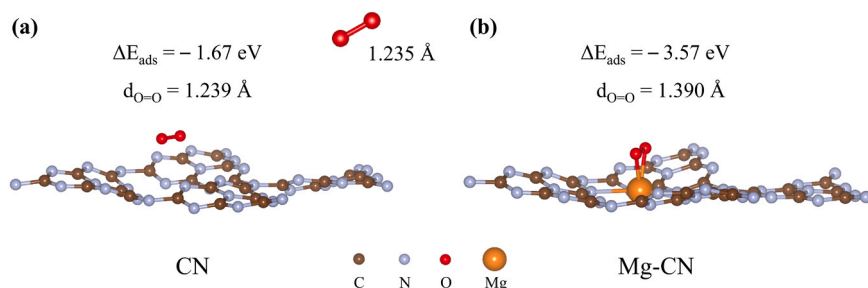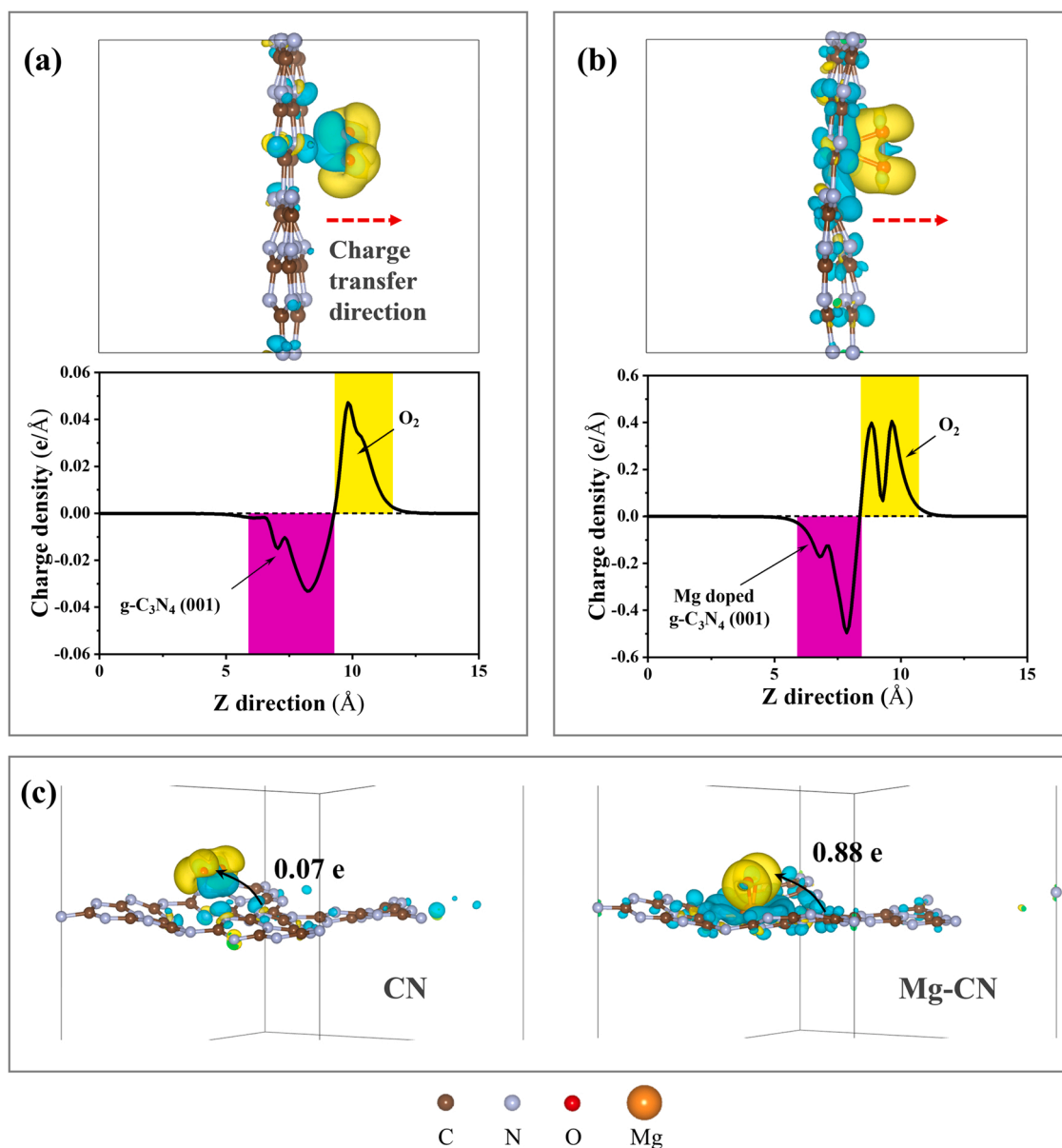

Fig. 6. Side view of CN (a) and Mg-CN (b) adsorbed with a O_2 molecule. The inset in (a) shows the free O_2 molecule model with a bond length of 1.235 Å.

Fig. 7. Comparison of charge difference distribution over CN (a) and Mg-CN (b) with adsorbed O$_2$. (c) Bader electron transfer over CN and Mg-CN with adsorbed O$_2$. (Charge accumulation and depletion are indicated in yellow and blue, respectively.).

charge accumulation and depletion, respectively. For both CN and Mg-CN, the electrons tend to transfer from g-C$_3$N$_4$ to O$_2$, as inferred by the plane average charge density difference along the Z direction (Figs. 7a and 7b). Specifically, the charge transfer number is 0.07 e for CN and 0.88 e for Mg-CN (Fig. 7c, S9, and S10), indicating an improved interaction between O$_2$ and catalyst substrate. Therefore, it can be expected that the presence of Mg SAs would play a significant role in facilitating ROSs production.

To further experimentally analyze the reactive species generation of catalysts, an ESR test was carried out. There was no reactive species signal that could be seen in dark conditions for both CN and 1.0Mg-CN. In contrast, under visible-light illumination, the signals of •O$_2^-$, •OH, and ^{1}O$_2$ were detected for both CN and 1.0Mg-CN (Fig. 8a-c). The increased signal of •O$_2^-$ radicals observed from 1.0Mg-CN is ascribed to the boosted adsorption and activation of O$_2$ molecules (Fig. 8a), as a result of electronic structure optimization and the resulting built-in electric field associated with the existence of Mg SAs. Additionally, 1.0Mg-CN showed the enhanced peak intensity of DMPO-•OH and TEMPO-^{1}O$_2$ in comparison to CN (Figs. 8b and 8c), due to the improved

electron excitation and charge transportation [48]. Based on the above reasoning, the photo-oxidation NO removal process on xMg-CN was proposed (Fig. 8d). To begin with, photoexcited electrons (e$^-$) and holes (h$^+$) are generated on 1.0Mg-CN under visible light irradiation (1.0Mg-CN + hν → e$^-$ + h$^+$). •O$_2^-$ radical is generated via the transfer of photoexcited electrons from the valence band to molecular oxygen (O$_2$ + e$^-$ → •O$_2^-$) [49–51]. Considering the redox potential of •OH/H$_2$O (+1.99 V) and the relatively negative valance band position of 1.0Mg-CN (+1.90 V) (Fig. S7), the formation pathway of •OH can be inferred to be •O$_2^-$ → H$_2$O$_2$ → •OH [52]. In addition, the generation of ^{1}O$_2$ is generally recognized to be associated with the oxidation of •O$_2^-$ by the photo-excited holes (•O$_2^-$ + h$^+$ → ^{1}O$_2$) [13,53]. Benefiting from the Mg introduction and the consequently optimized electronic microenvironment, the activation of O$_2$ and the separation/transfer of photoinduced charge carriers are greatly improved; as a result, boosted ROSs (•O$_2^-$, ^{1}O$_2$, •OH) generation can be realized. Under the attack of the enhanced ROSs, notably enhanced NO removal activity is obtained; meanwhile, NO can be easily oxidized in depth to the final product (e.g., nitrate) rather than the toxic intermediate (NO$_2$).
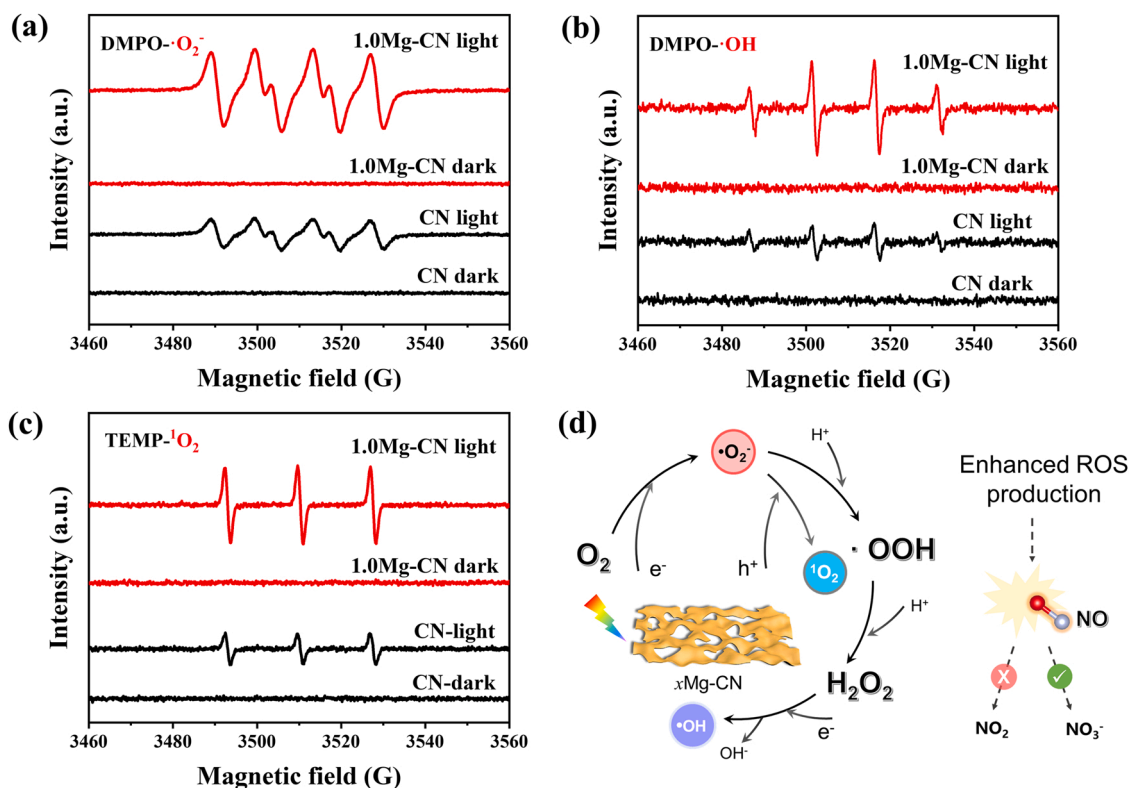
Fig. 8. ESR spectra of reactive oxygen species trapping for (a) $\bullet O_2^-$, (b) $\bullet OH$, and (c) $^1O_2$ over CN and 1.0Mg-CN. (d) Proposed photocatalytic NO oxidation mechanism over 1.0Mg-CN catalyst.

4. Conclusion

To summarize, a Mg-SAs modified g-C$_3$N$_4$ nanosheet photocatalyst was prepared via a facile calcination method with MgCl$_2$•6H$_2$O hydrothermally pretreated dicyandiamide as the precursor. The 1.0Mg-CN catalyst presented excellent photocatalytic NO purification activity with a NO removal rate of 52.3% within 30 min, far surpassing the value of the Mg-free analog (CN, 41.2%). Meanwhile, the production rate of toxic intermediate NO$_2$ over 1.0Mg-CN was inhibited to a certain extent, as compared to CN. The excellent NO photo-oxidation performance of 1.0Mg-CN mainly originated from the optimization of the electronic structure caused by the existence of Mg SAs; concretely, Mg SAs manipulated the charge distribution and introduced a locally built-in electric field, which was beneficial for the fast photo-excited charge transfer kinetics. Additionally, theoretical calculations revealed that the presence of Mg SAs favored the activation and adsorption of O$_2$ over g-C$_3$N$_4$. For the above reasons, photo-induced ROSs production was substantially boosted. Under the attack of adequate ROSs, the NO was easily oxidized to nitrate instead of the toxic intermediate (NO$_2$). The insight into the significant roles of Mg single-atom units would inspire the design of more efficient g-C$_3$N$_4$-based catalysts for air purification.

CRediT authorship contribution statement

Kaining Li: Writing – original draft, Methodology, Conceptualization. **Yasutaka Kuwahara:** Writing – review & editing, Supervision. **Zhi Wang:** Investigation. **Xiaofang Li:** Methodology, Data curation. **Ningxin Kang:** Investigation, Data curation. **Ning Wang:** Data curation, Investigation. **Hiromi Yamashita:** Writing – review & editing, Supervision. **Kangle Lv:** Writing – review & editing, Supervision.

Declaration of Competing Interest

The authors declare the following financial interests/personal relationships which may be considered as potential competing interests: The corresponding author of this manuscript, Prof. Hiromi Yamashita, is one of the editorial members of this journal. If there are other authors, they declare that they have no known competing financial interests or personal relationships that could have appeared to influence the work reported in this paper.

Data Availability

Data will be made available on request.

Appendix A. Supporting information

Supplementary data associated with this article can be found in the online version at doi:10.1016/j.apcatb.2024.124163.

References

[1] L. Han, S. Cai, M. Gao, J.Y. Hasegawa, P. Wang, J. Zhang, L. Shi, D. Zhang, Selective catalytic reduction of NO$_x$ with NH$_3$ by using novel catalysts: State of the art and future prospects, Chem. Rev. 119 (2019), 10916–10976.

[2] S. Deutz, D. Bongartz, B. Heuser, A. Kätelhön, L. Schulze Langenhorst, A. Omari, M. Walters, J. Klankermayer, W. Leitner, A. Mitsos, S. Pischinger, A. Bardow, Cleaner production of cleaner fuels: wind-to-wheel-environmental assessment of CO$_2$-based oxymethylene ether as a drop-in fuel, Energy Environ. Sci. 11 (2018) 331–343.

[3] Y. Lei, C. Qin, T. Qiu, G. Yue, M. Ding, NO_x emission removal from a parallel diesel engine group by SCR system based on distributed control technology, Environ. Sci. Technol. 55 (2021) 6352–6362.

[4] C. Misra, C. Ruehl, J. Collins, D. Chernich, J. Herner, In-use NO_x emissions from diesel and liquefied natural gas refuse trucks equipped with SCR and TWC, respectively, Environ. Sci. Technol. 51 (2017) 6981–6989.

[5] D. Liu, D. Chen, N. Li, Q. Xu, H. Li, J. He, J. Lu, Surface engineering of g-C_3N_4 by stacked BiOBr sheets rich in oxygen vacancies for boosting photocatalytic performance, Angew. Chem. Int. Ed. 59 (2020) 4519–4524.

[6] Y. Duan, Y. Wang, L. Gan, J. Meng, Y. Feng, K. Wang, K. Zhou, C. Wang, X. Han, X. Zhou, Amorphous carbon nitride with three coordinate nitrogen (N_3C) vacancies for exceptional NO_x abatement in visible light, Adv. Energy Mater. 11 (2021) 2004001.

[7] J. Ma, C. Wang, H. He, Enhanced photocatalytic oxidation of NO over g-C_3N_4-TiO_2 under UV and visible light, Appl. Catal. B Environ. 184 (2016) 28–34.

[8] Y. Ren, Y. Li, X. Wu, J. Wang, G. Zhang, S-scheme Sb_2WO_6/g-C_3N_4 photocatalysts with enhanced visible-light-induced photocatalytic NO oxidation performance, Chin. J. Catal. 42 (2021) 69–77.

[9] W. Cui, J. Li, F. Dong, Y. Sun, G. Jiang, W. Cen, S.C. Lee, Z. Wu, Highly efficient performance and conversion pathway of photocatalytic NO oxidation on SrO-Clusters@Amorphous carbon nitride, Environ. Sci. Technol. 51 (2017), 10682–10690.

[10] Y. Li, M. Gu, X. Zhang, J. Fan, K. Lv, S.A.C. Carabineiro, F. Dong, 2D g-C_3N_4 for advancement of photo-generated carrier dynamics: status and challenges, Mater. Today 41 (2020) 270–303.

[11] T. Xiong, W. Cen, Y. Zhang, F. Dong, Bridging the g-C_3N_4 interlayers for enhanced photocatalysis, ACS Catal. 6 (2016) 2462–2472.

[12] J. Li, Z. Zhang, W. Cui, H. Wang, W. Cen, G. Johnson, G. Jiang, S. Zhang, F. Dong, The spatially oriented charge flow and photocatalysis mechanism on internal van der Waals heterostructures enhanced g-C_3N_4, ACS Catal. 8 (2018) 8376–8385.

[13] K. Li, W. Zhou, X. Li, Q. Li, S.A.C. Carabineiro, S. Zhang, J. Fan, K. Lv, Synergistic effect of cyano defects and $CaCO_3$ in graphitic carbon nitride nanosheets for efficient visible-light-driven photocatalytic NO, Remov., J. Hazard. Mater. 442 (2023) 130040.

[14] X. Zhang, H. Su, P. Cui, Y. Cao, Z. Teng, Q. Zhang, Y. Wang, Y. Feng, R. Feng, J. Hou, X. Zhou, P. Ma, H. Hu, K. Wang, C. Wang, L. Gan, Y. Zhao, Q. Liu, T. Zhang, K. Zheng, Developing Ni single-atom sites in carbon nitride for efficient photocatalytic H_2O_2 production, Nat. Commun. 14 (2023) 7115.

[15] J. Shen, C. Luo, S. Qiao, Y. Chen, Y. Tang, J. Xu, K. Fu, D. Yuan, H. Tang, H. Zhang, C. Liu, Single-atom Cu channel and N-vacancy engineering enables efficient charge separation and transfer between C_3N_4 interlayers for boosting photocatalytic hydrogen production, ACS Catal. 13 (2023) 6280–6288.

[16] Q. Yang, T. Wang, Z. Zheng, B. Xing, C. Li, B. Li, Constructing interfacial active sites in Ru/g-C_3N_{4-x} photocatalyst for boosting H_2 evolution coupled with selective benzyl-alcohol oxidation, Appl. Catal. B Environ. 315 (2022) 121575.

[17] L. Cheng, H. Yin, C. Cai, J. Fan, Q. Xiang, Single Ni atoms anchored on porous few-layer g-C_3N_4 for photocatalytic CO_2 reduction: The role of edge confinement, Small 16 (2020) 2002411.

[18] S. Hu, P. Qiao, X. Yi, Y. Lei, H. Hu, J. Ye, D. Wang, Selective photocatalytic reduction of CO_2 to CO mediated by silver single atoms anchored on tubular carbon nitride, Angew. Chem. Int. Ed. 62 (2023) e202304585.

[19] M. Ou, S. Wan, Q. Zhong, S. Zhang, Y. Wang, Single Pt atoms deposition on g-C_3N_4 nanosheets for photocatalytic H_2 evolution or NO oxidation under visible light, Int. J. Hydrog. Energy 42 (2017) 27043–27054.

[20] G. Liu, Y. Huang, H. Lv, H. Wang, Y. Zeng, M. Yuan, Q. Meng, C. Wang, Confining single-atom Pd on g-C_3N_4 with carbon vacancies towards enhanced photocatalytic NO conversion, Appl. Catal. B Environ. 284 (2021) 119683.

[21] Q. Wang, K. Liu, J. Fu, C. Cai, H. Li, Y. Long, S. Chen, B. Liu, H. Li, W. Li, X. Qiu, N. Zhang, J. Hu, H. Pan, M. Liu, Atomically dispersed s-block magnesium sites for electroreduction of CO_2 to CO, Angew. Chem. Int. Ed. 60 (2021), 25241–25245.

[22] X. Dong, S. Zhang, H. Wu, Z. Kang, L. Wang, Facile one-pot synthesis of Mg-doped g-C_3N_4 for photocatalytic reduction of CO_2, RSC Adv. 9 (2019), 28894–28901.

[23] W. Yan, L. Yan, C. Jing, Impact of doped metals on urea-derived g-C_3N_4 for photocatalytic degradation of antibiotics: Structure, photoactivity and degradation mechanisms, Appl. Catal. B Environ. 244 (2019) 475–485.

[24] C.H. Shin, H.Y. Lee, C. Gyan-Barimah, J.H. Yu, J.S. Yu, Magnesium: properties and rich chemistry for new material synthesis and energy applications, Chem. Soc. Rev. 52 (2023) 2145–2192.

[25] S. Liu, Z. Li, C. Wang, W. Tao, M. Huang, M. Zuo, Y. Yang, K. Yang, L. Zhang, S. Chen, P. Xu, Q. Chen, Turning main-group element magnesium into a highly active electrocatalyst for oxygen reduction reaction, Nat. Commun. 11 (2020) 938.

[26] Y. Wang, P. Du, H. Pan, L. Fu, Y. Zhang, J. Chen, Y. Du, N. Tang, G. Liu, Increasing solar absorption of atomically thin 2D carbon nitride sheets for enhanced visible-light photocatalysis, Adv. Mater. 31 (2019) 1807540.

[27] J. Cheng, Z. Hu, K. Lv, X. Wu, Q. Li, Y. Li, X. Li, J. Sun, Drastic promoting the visible photoreactivity of layered carbon nitride by polymerization of dicyandiamide at high pressure, Appl. Catal. B Environ. 232 (2018) 330–339.

[28] X. Li, K. Li, D. Ding, J. Yan, C. Wang, S.A.C. Carabineiro, Y. Liu, K. Lv, Effect of oxygen vacancies on the photocatalytic activity of flower-like BiOBr microspheres towards NO oxidation and CO_2 reduction, Sep. Purif. Technol. 309 (2023) 123054.

[29] X. Li, Z. Hu, Q. Li, M. Lei, J. Fan, S.A.C. Carabineiro, Y. Liu, K. Lv, Three in one: Atomically dispersed Na boosting the photoreactivity of carbon nitride towards NO oxidation, Chem. Commun. 56 (2020) 14195–14198.

[30] J. Li, X. Dong, Y. Sun, G. Jiang, Y. Chu, S.C. Lee, F. Dong, Tailoring the rate-determining step in photocatalysis via localized excess electrons for efficient and safe air cleaning, Appl. Catal. B Environ. 239 (2018) 187–195.

[31] M.G. Jeong, S.Y. Kim, D.H. Kim, S.W. Han, I.H. Kim, M. Lee, Y.K. Hwang, Y.D. Kim, High-performing and durable MgO/Ni catalysts via atomic layer deposition for CO_2 reforming of methane (CRM), Appl. Catal. A Gen. 515 (2016) 45–50.

[32] S. Dong, Y. Zhao, J. Yang, W. Li, W. Luo, S. Li, X. Liu, H. Guo, C. Yu, J. Sun, J. Feng, Y. Zhu, Solar water recycling of carbonaceous aerogel in open and colsed systems for seawater desalination and wastewater purification, Chem. Eng. J. 431 (2022) 133824.

[33] X. Wu, H. Ma, W. Zhong, J. Fan, H. Yu, Porous crystalline g-C_3N_4: Bifunctional $NaHCO_3$ template-mediated synthesis and improved photocatalytic H_2-evolution rate, Appl. Catal. B Environ. 271 (2020) 118899.

[34] L. Chen, C. Chen, Z. Yang, S. Li, C. Chu, B. Chen, Simultaneously tuning band structure and oxygen reduction pathway toward high-efficient photocatalytic hydrogen peroxide production using cyano-rich graphitic carbon nitride, Adv. Funct. Mater. 31 (2021) 2105731.

[35] W. Wang, H. Zhang, S. Zhang, Y. Liu, G. Wang, C. Sun, H. Zhao, Potassium-ion-assisted regeneration of active cyano groups in carbon nitride nanoribbons: Visible-light-driven photocatalytic nitrogen reduction, Angew. Chem. Int. Ed. 58 (2019) 16644–16650.

[36] M. Gao, J. Yang, T. Sun, Z. Zhang, D. Zhang, H. Huang, H. Lin, Y. Fang, X. Wang, Persian buttercup-like $BiOBr_xCl_{1-x}$ solid solution for photocatalytic overall CO_2 reduction to CO and O_2, Appl. Catal. B Environ. 243 (2019) 734–740.

[37] Q. Tan, K. Li, Q. Li, Y. Ding, J. Fan, Z. Xu, K. Lv, Photosensitization of TiO_2 nanosheets with $ZnIn_2S_4$ for enhanced visible photocatalytic activity toward hydrogen production, Mater. Today Chem. 26 (2022) 101114.

[38] K. Li, Y. Kuwahara, H. Yamashita, Aminopolymer-functionalized hollow carbon spheres incorporating Ag nanoparticles for electrochemical syngas production from CO_2, Appl. Catal. B Environ. 331 (2023) 122713.

[39] S. Dong, X. Liu, G. Tian, Y. Wang, J. Zhao, J. Sun, M. Fan, Surface oxygen vacancies modified Bi_2MoO_6 double-layer spheres: Enhanced visible LED light photocatalytic activity for ciprofloxacin degradation, J. Alloy. Compd. 892 (2022) 162217.

[40] X. Wang, S. Zhang, X. Li, Z. Zhan, B. Tan, X. Lang, S. Jin, Two-dimensional crystalline covalent triazine frameworksviadual modulator control for efficient photocatalytic oxidation of sulfides, J. Mater. Chem. A. 9 (2021), 16405–16410.

[41] C. Wu, W. Huang, H. Liu, K. Lv, Q. Li, Insight into synergistic effect of Ti_3C_2 MXene and MoS_2 on anti-photocorrosion and photocatalytic of CdS for hydrogen production, Appl. Catal. B Environ. 330 (2023) 122653.

[42] Y. Li, M. Gu, M. Zhang, X. Zhang, K. Lv, Y. Liu, W. Ho, F. Dong, C_3N_4 with engineered three coordinated (N_3C) nitrogen vacancy boosts the production of $^1O_2$ for Efficient and stable NO photo-oxidation, Chem. Eng. J. 389 (2020) 124421.

[43] C. Liu, Q. Ma, Y. Liu, J. Ma, H. He, Synergistic reaction between SO_2 and NO_2 on mineral oxides: A potential formation pathway of sulfate aerosol, Phys. Chem. Chem. Phys. 14 (2012) 1668–1676.

[44] X. Shi, P. Wang, W. Li, Y. Bai, H. Xie, Y. Zhou, L. Ye, Change in photocatalytic NO removal mechanisms of ultrathin BiOBr/BiOI via NO_3^- adsorption, Appl. Catal. B Environ. 243 (2019) 322–329.

[45] Q. Wang, K. Zhang, S. Zheng, X. Hu, L. Wang, H. Du, G. Yang, An innovative AgI/MIL-100(Fe) Z-scheme heterojunction for simultaneously enhanced photoreduction of Cr(VI) and antibacterial activity, Appl. Surf. Sci. 616 (2023) 156528.

[46] K. Li, W. Cui, J. Li, Y. Sun, Y. Chu, G. Jiang, Y. Zhou, Y. Zhang, F. Dong, Tuning the reaction pathway of photocatalytic NO oxidation process to control the secondary pollution on monodisperse Au nanoparticles@g-C_3N_4, Chem. Eng. J. 378 (2019) 122184.

[47] W. Cui, W. Yang, P. Chen, L. Chen, J. Li, Y. Sun, Y. Zhou, F. Dong, Earth-abundant $CaCO_3$-based photocatalyst for enhanced ROS production, toxic by-product suppression, and efficient NO removal, Energy Environ. Mater. 5 (2022) 928–934.

[48] S. Dong, X. Yan, W. Li, Y. Liu, X. Han, X. Liu, J. Feng, C. Yu, C. Zhang, J. Sun, Macroscopic Zn-doped α-Fe_2O_3/graphene aerogel mediated persulfate activation for heterogeneous catalytic degradation of sulfamonomethoxine wastewater, J. Ind. Eng. Chem. 108 (2022) 254–262.

[49] Q. Wang, L. Wang, S. Zheng, M. Tan, L. Yang, Y. Fu, Q. Li, H. Du, G. Yang, The strong interaction and confinement effect of Ag@NH_2-MIL-88B for improving the conversion and durability of photocatalytic Cr(VI) reduction in the presence of a hole scavenger, J. Hazard. Mater. 451 (2023) 131149.

[50] X. Li, S. Lyu, X. Lang, Superoxide generated by blue light photocatalysis of g-C_3N_4/TiO_2 for selective conversion of amines, Environ. Res. 195 (2021) 110851.

[51] J. Guo, D. Ma, F. Sun, G. Zhuang, Q. Wang, A.M. Al-Enizi, A. Nafady, S. Ma, Substituent engineering in g-C_3N_4/COF heterojunctions for rapid charge separation and high photo-redox activity, Sci. China Chem. 65 (2022) 1704–1709.

[52] W. Cui, J. Li, Y. Sun, H. Wang, G. Jiang, S.C. Lee, F. Dong, Enhancing ROS generation and suppressing toxic intermediate production in photocatalytic NO oxidation on O/Ba co-functionalized amorphous carbon nitride, Appl. Catal. B Environ. 237 (2018) 938–946.

[53] M. Gu, Y. Yang, L. Zhang, B. Zhu, G. Liang, J. Yu, Efficient sacrificial-agent-free solar H_2O_2 production over all-inorganic S-scheme composites, Appl. Catal. B Environ. 324 (2023) 122227.